

AD-A264 440

ITATION PAGE

Form Approved
OMB No. 0704-0188

(2)

Page 1 hour per response, including the time for reviewing instructions, searching existing data sources, gathering and maintaining the data needed, and completing and reviewing the collection of information. Send comments regarding this burden or any other aspect of this collection of information, including suggestions for reducing burden, to Information Operations and Reports, 1215 Jefferson Davis Highway, Suite 1204, Arlington, VA 22202-4302, and to OMB No. 0704-0188, Washington, DC 20503.

3. Report Type and Dates Covered. Final - Journal Article	1. Date. 1993		
4. Title and Subtitle. Evaluation of Multichannel Wiener Filters Applied to Fine Resolution Passive Microwave Images of First-Year Sea Ice			
6. Author(s). William E. Full* and Duane T. Epple			
7. Performing Organization Name(s) and Address(es). Naval Research Laboratory Ocean Science Directorate Stennis Space Center, MS 39529-5004			
9. Sponsoring/Monitoring Agency Name(s) and Address(es). Naval Research Laboratory Basic Research Management Office Stennis Space Center, MS 39529-5004			
11. Supplementary Notes. Published in Remote Sens. Environ. *Wichita State University, Kansas			
12a. Distribution/Availability Statement. Approved for public release; distribution is unlimited.			
12b. Distribution Code.			
13. Abstract (Maximum 200 words). Over the past two decades passive microwave imaging systems have proved to be effective reconnaissance tools in polar environments. However, the mechanical scan mechanism and high gain electronics characteristic of this class of sensors commonly impart noise and unwanted artifacts to image data they produce, complicating visual analysis and automated classification procedures. The fact that data in individual scan lines are characterized by statistical stationarity and that information in adjacent pixels is highly correlated due to oversampling of these image data suggests that Wiener multichannel filtering techniques may prove effective in this application. Wiener filters applied to passive microwave images of first-year sea ice were constructed. Four major parameters that define the filter (lag or pixel offset between the original and desired scenes, filter length, number of lines in the filter, and weight applied to the empirical correlation functions) were varied. Results were compared visually to assess the effect of each variable on image quality. Effective filters that limit high frequency noise and enhance ice characteristics use a lag of one pixel, consist of two or three channels, are five pixels in length, and weigh the auto- and cross-correlation functions equally.			
14. Subject Terms. Sea ice classification, passive microwave, remote sensing			
15. Number of Pages. 23			
16. Price Code.			
17. Security Classification of Report. Unclassified	18. Security Classification of This Page. Unclassified	19. Security Classification of Abstract. Unclassified	20. Limitation of Abstract. SAR

DTIC
S ELECTE
MAY 1 3 1993
C D

93 5 10 003

93-10206

DTIC QUALITY INSPECTED 1

Accession For		
NTIS	CRA&I	<input type="checkbox"/>
DTIC	TAB	<input type="checkbox"/>
Unannounced		<input type="checkbox"/>
Justification		
By		
Distribution		
Availability Codes		
Avail and/or Special		
		A.I 20

Evaluation of Multichannel Wiener Filters Applied to Fine Resolution Passive Microwave Images of First-Year Sea Ice

William E. Full

FIMTSI, Department of Geology, Wichita State University, Kansas

Duane T. Eppler

Polar Oceanography Branch Office, Naval Oceanographic and Atmospheric Research Laboratory,
Hanover, New Hampshire

Over the past two decades passive microwave imaging systems have proven to be effective reconnaissance tools in polar environments. However, the mechanical scan mechanism and high gain electronics characteristic of this class of sensors commonly impart noise and unwanted artifacts to image data they produce, complicating visual analysis and automated classification procedures. The fact that data in individual scan lines are characterized by statistical stationarity and that information in adjacent pixels is highly correlated due to oversampling of these image data suggests that Wiener multichannel filtering techniques may prove effective in this application. Wiener filters applied to passive microwave images of first-year sea ice were constructed. Four major parameters that define the filter (lag or pixel offset between the original and desired scenes, filter length, number of lines in the filter, and weight applied to the empirical correlation functions) were varied. Results were compared visually to assess the effect of each variable on image quality. Effective filters

that limit high frequency noise and enhance ice characteristics use a lag of one pixel, consist of two or three channels, are five pixels in length, and weigh the auto- and cross-correlation functions equally.

INTRODUCTION

Passive microwave imaging systems represent one component of a balanced, multisensor instrument suite that is required to characterize the sea ice cover in polar regions. A series of field experiments extending over almost 2 decades involving surface investigations and aircraft overflights established the utility of passive microwave data in assessing the relative age of sea ice, its geographic extent and concentration, the location of water openings, and the dynamic structure of the polar ice pack (Campbell et al., 1975; 1976; 1978; Hollinger et al., 1984; Eppler et al., 1986; Cavalieri et al., 1986). The overall results of these missions demonstrate that aircraft passive microwave images of high quality are of significant value to programs that involve reconnaissance, operations, and research in polar environments.

Address correspondence to William E. Full, FIMTSI, Dept. of Geology, Wichita State Univ., Wichita, KS 67260-0027.

Received 30 November 1991; revised 16 July 1992.

Aircraft sensors constructed to provide fine resolution passive microwave imagery typically employ a scanning antenna assembly to measure the extremely weak (10^{-14} W) microwave signal emanating from the earth's surface (Hollinger et al., 1976; Eppler and Heydlauff, 1990). High gain

electronics amplify the signal and pass it to recording and display systems in the aircraft cabin. Both the mechanical scan mechanism and high gain electronics commonly impart undesirable artifacts to the data that complicate both automated classification procedures applied to derive ice

Figure 1. KRMS image of first-year sea ice. The scene is 512×512 pixels in size and shows an area approximately 14.5 km across. The image was acquired from an altitude of 6100 m (20,000 ft) on 11 March 1988 in the Beaufort Sea 200 km from the Alaskan coast near $71^{\circ}45'N$ $144^{\circ}30'W$. Surfaces shown range in brightness temperature from approximately 215 K to 242 K. Dark areas are radiometrically warm and indicate ice that is highly emissive at the sensor frequency (33.6 GHz); light areas are radiometrically cool. The mottled pattern is typical of first-year ice in this region and reflects variation in surface properties of the ice surface and overlying snow.



type distributions (Hoyer, 1990; Eppler et al., 1986; Eppler and Farmer, 1991b) and, to a lesser degree, visual analysis of the images. Electronic artifacts, which arise from noise introduced when the weak radiometer signal is amplified, impart a snowy appearance to the image (Fig. 1). This adds to variance associated with intensities typical of different surface types and increases the probability that pixels will be misclassified when segmentation techniques are applied (Eppler et al., 1986), especially those associated with automated classification systems. Scan artifacts, which consist of magnitude shifts in signal intensity and in lateral shifts in feature location from scan to scan, arise from imbalance between antennas and from timing aberrations that occur during data transfer and storage. This results in each scan being classified as an edge when texture classifiers based on gradient and edge detection logic are applied to the image (Eppler and Farmer, 1991b).

Work described here reports results of applying multichannel Wiener filtering techniques to minimize electronic noise imparted to fine resolution passive microwave sea ice images by high-gain sensor electronics. In particular, we apply the method to images of first-year sea ice, which show subtle patterns of variation in surface emissivity (Figs. 1 and 2). These patterns, which are particularly susceptible to obscuration by instru-

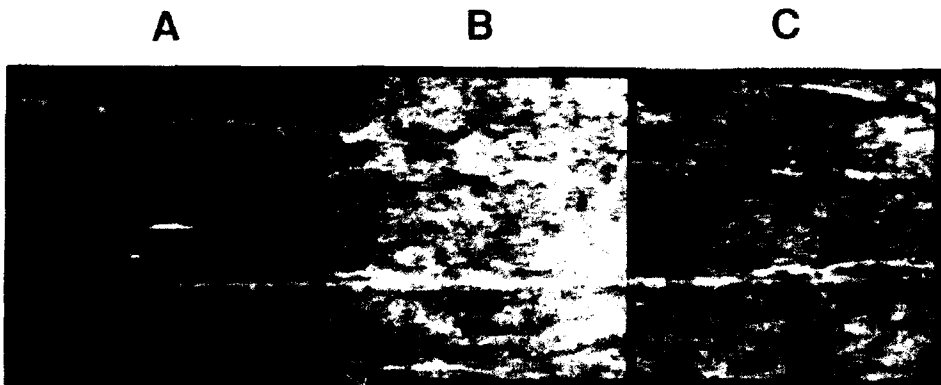
ment noise, are important from a scientific perspective because they reflect areal variation in physical characteristics of snow and ice.

Image data used to evaluate the filter were obtained with the U.S. Navy K_a-band Radiometric Mapping System (KRMS), an aircraft sensor that acquires high resolution passive microwave imagery at a frequency of 33.6 GHz (Eppler et al., 1984; 1986; Eppler and Heydlauff, 1990). Our objectives in applying the filter are to improve visual clarity of the images so that ice variability may be mapped, and to enhance the effectiveness of automated image classification techniques by noise reduction. As will be shown below, use of Wiener signal enhancement filters is appropriate in this application as a natural consequence of the structure of data acquired with a scanning sensor.

BACKGROUND

Traditional methods of dealing with noise reduction use various smoothing filters or applications of the Fourier transform functions. Several of the traditional techniques were applied to passive microwave imagery, largely with unsatisfactory results. For example, consider the results of applying a moving average function (convolution) to the three images of first-year sea ice in Figure

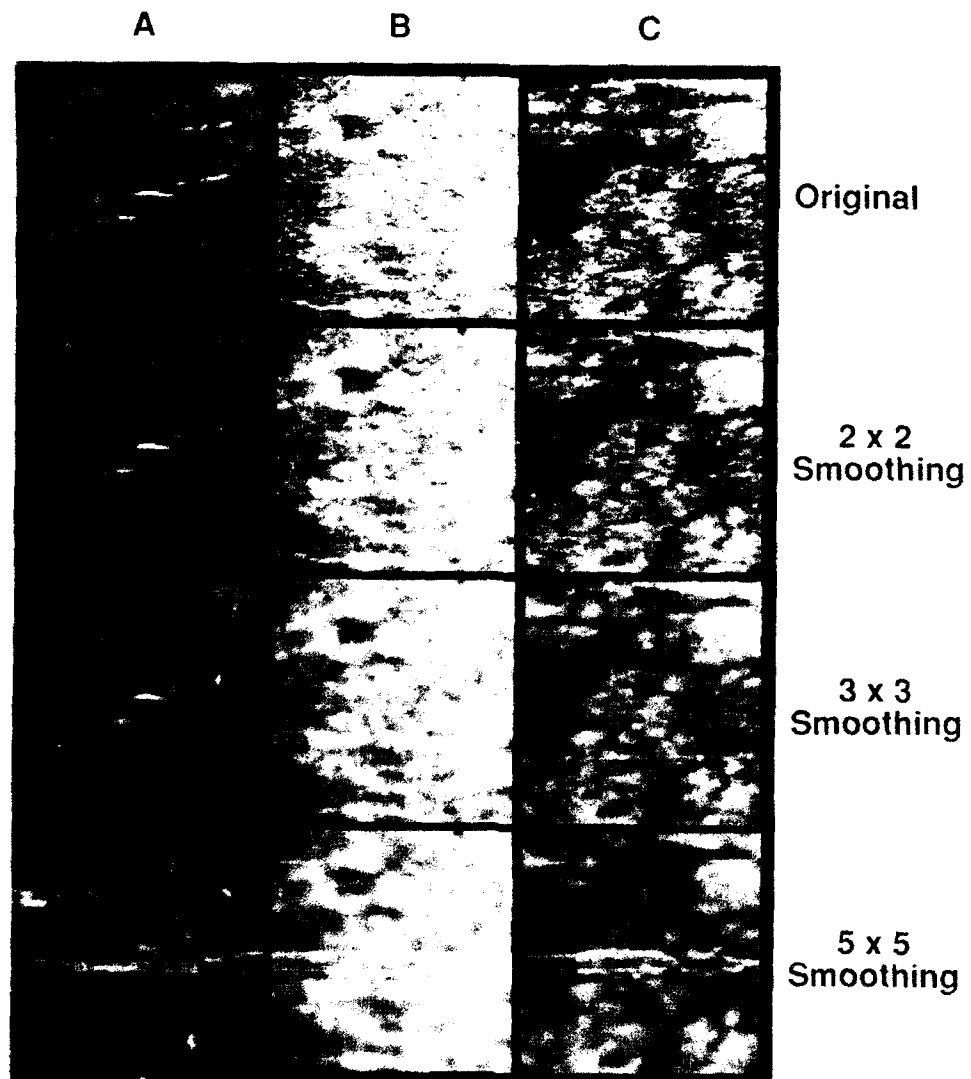
Figure 2. KRMS test images used in this study. Two of the images (B and C) show first-year sea ice exclusively. The third image (A) consists predominantly of first-year ice, but also shows a break in the ice cover (bright streak at center of image in first column) that exposes sea water, which is radiometrically cold. This image (A) was included to test the degree to which the Wiener filter technique is robust with respect to high-contrast features that occur in an otherwise low-contrast scene. Each image is 128 × 128 pixels in size. The test images are composed of scans acquired with only one of KRMS's three antennas and so are foreshortened in the downtrack direction. The area shown by each test image is approximately 3.6 km across and 10.9 km from top to bottom. Histogram equalization and range transformation were also performed over all three images.



2. Three moving average functions, 2×2 , 3×3 , and 5×5 , were used to produce the filtered images in Figure 3. Convolution reduces noise and eliminates the snowy appearance of the original image, but at the expense of high frequency information. Information removed by the filter can be displayed in image form by subtracting the filtered image from the original image (Fig. 4). These image difference maps are convenient for visually presenting the net change in an image due to a filter operator (original image \approx convolved image + difference image). Note in Figure 3 that features become fuzzy as a result of applying these

filters. This blurring is unacceptable because textural and edge information is being removed (Fig. 4) that might be useful in subsequent analytical processing. Figure 4 captures these regions of greatest smoothing as ghostlike features on an otherwise featureless background. We seek to preserve this high-frequency information while removing the noise, and standard convolution methods (Rush, 1990) have failed with this data. Application of other filters such as the double Fourier transform (Gonzales and Wintz, 1977; Rush, 1990) failed also to provide the desired enhancement, probably due to the fact that noise

Figure 3. Images in Figure 2 (labeled original in this and subsequent figures) convolved with 2×2 , 3×3 , and 5×5 smoothing kernels. Note the increased blurring of subtle textural features and the obscuration of feature edges by operators of increasing size. All the images in Figures 3 and 4, along with all subsequent images, are presented histogram equalized and range expanded to maximize the visual impact of subtle features.



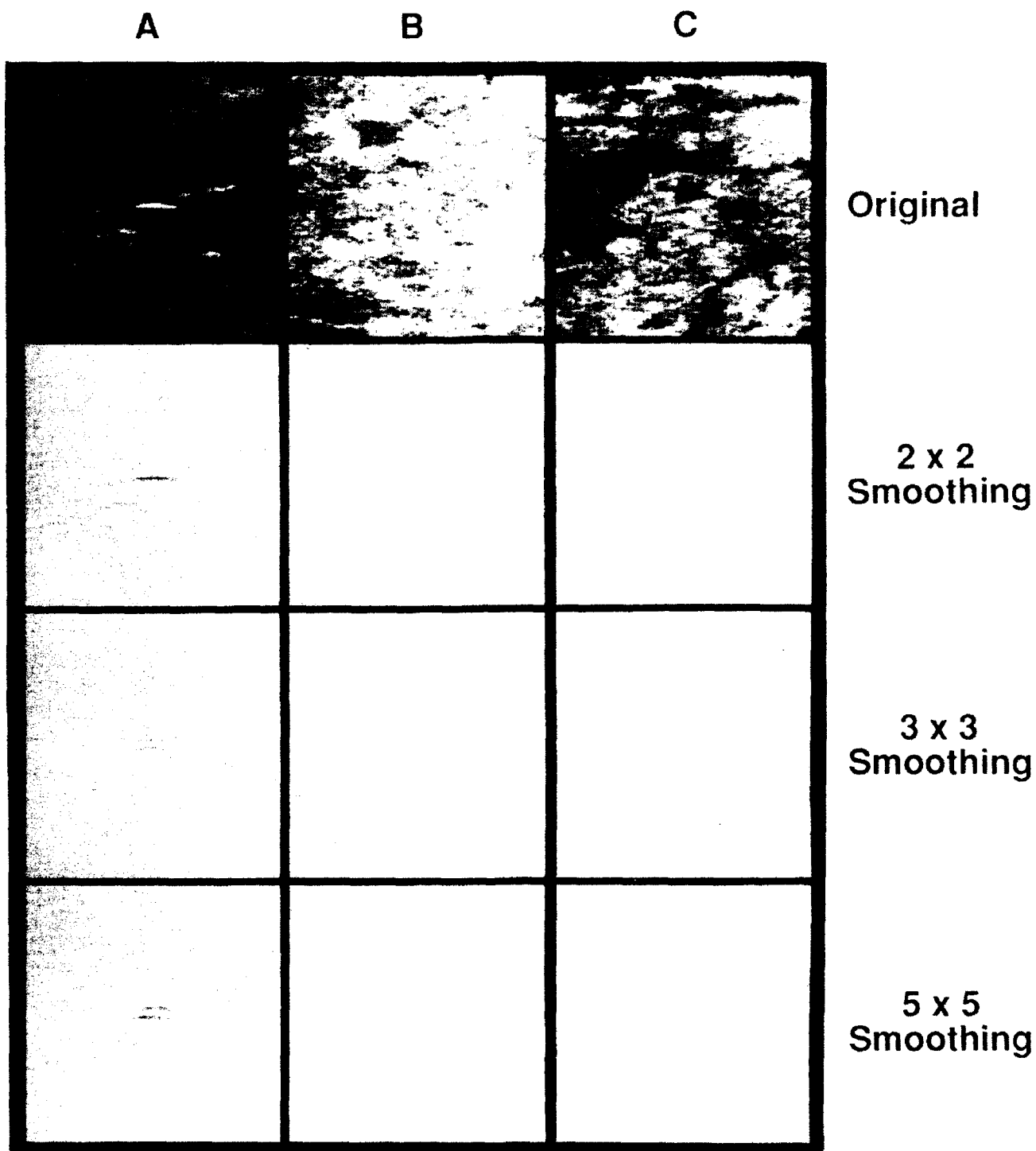


Figure 4. Difference images derived by subtracting the convolved images shown in previous figure from the original images (first row of images), histogram equalized, and range transformed. Features undergoing the greatest change will be displayed as dominant features in these images. Note the relatively uniform texture except where relatively abrupt changes in intensity occur.

present in the images is not arrayed within distinct spatial frequencies which are necessary to define effective Fourier filters. Other less popular approaches were tried with similarly disappointing lack of success.

WIENER ENHANCEMENT FILTERING

Most current theories for prediction and enhancement of time series signals are based on the original work of Norbert Wiener (Wiener, 1942). Wiener was interested in the systematic design of filters to enhance signals and minimize unwanted noise in time series analysis. In particular, Wiener desired to design filters that could be used for signal prediction and forecasting. Some of the earliest applications of Wiener's work involved long-range weather forecasting during the Second World War. Most current applications of this form of analysis concern separation of desired signals from unwanted noise in seismic signal analysis (Robinson, 1983).

Examples of the extension of Wiener theory to multiple channels are numerous and span diverse research fields. One of the more recent nonseismic applications is reported in Williams et al. (1988), who discuss applications for multivariate data including atmospheric isotopic variations through earth history. In multivariate applications such as these, each of the channels is assumed to record similar events in time which have been corrupted by noise that is uncorrelatable across channels. Wiener filters are applied to enhance correlative events and subdue noise manifest by uncorrelatable events observed across channels. Wiener-type theory also has been widely used for image restoration (Gonzalez and Wintz, 1977; Rosenfeld and Kak, 1982; Rush, 1990), although the manner in which we apply these filters here is derived more from seismic literature (Robinson and Treitel, 1980; Robinson, 1983; Robinson and Durrani, 1986) and its extension into the multichannel domain (Williams et al., 1988) than from conventional methods of image restoration.

In the current application we consider imagery acquired by scanning sensors to be analogous to time series data. Rows or columns of pixel intensities, which represent time-dependent measurements acquired by the sensor antenna as it sweeps across the imaged field of view, form the

time-varying signal to be filtered. Adjacent scans (rows or columns) contain similar information that is highly correlated for two reasons. First, adjacent scans carry redundant information because scanner data, if acquired properly, are oversampled to satisfy Nyquist criteria. Second, different parts of features that span more than one scan appear at similar points in adjacent scans (Fig. 5). Application of Wiener multichannel techniques provides a means of a) enhancing edges, features, and patterns that appear in adjacent scans and that are highly correlated with respect to position in the scan and b) minimizing the effect of noise that is not correlated between scans.

Multichannel Wiener filtering is described elsewhere in detail (Rosenfeld and Kak, 1982; Robinson, 1983). Principles that underlie this type of filtering are summarized below so that assumptions inherent in correct application of the method are clear. The notation of Robinson (1983) will be used in this discussion, and it will be cast in terms of image data addressed by this study.

Wiener filtering procedures are based on least-squares techniques. The least-squares class of filters depends on the existence of correlations between the actual and the desired scene to define an optimal filter, which is used to convolve the actual scene into the desired scene. Let us define the input scene as X_{mn} and the desired output as Z_{mn} , where m represents the time-sampled raster scan (row or column of pixels) and n represents the number of scan lines that we wish to be included in the Wiener filter. Correlations should exist among the information expressed by the family of n scan-lines chosen. Note that if the noise spectra were correlated with the signal, then that portion of the noise would be considered as signal in this analysis, potentially amplifying undesired effects. However, as noted in the next section, the noise we are trying to remove is not correlatable to the signal in the images used in this study. We define the standard autocorrelation function of the input for each scan line n as

$$\Phi_{rj}(\tau) = E\{x_{mj}x_{(m-\tau)j}^T\}, \quad \tau = 0, 1, 2, \dots, \quad (1)$$

where $\Phi_{rj}(\tau)$ represents the autocorrelation function of raster scan j ($1 \leq j \leq n$) over m pixels and for pixel lags (τ) $0, 1, 2, \dots$ and so forth, and E represents the usual recipe for calculating the autocorrelation of raster scan x_{mj} in terms of the line itself and its transpose defined at various lags.

The T represents the standard transpose function. In our case, $m + \tau =$ total number of pixels in the original raster scan. That is, X_{mn} represents the image defined by pixels 1, 2, ..., m for the first n scan lines while Z_{mn} is the image defined by pixels, $\tau, \tau + 1, \dots, m + \tau$, for the same n scan lines of the original image. Similarly, the cross-correlation function can be defined as

$$\Phi_{zrj}(\tau) = E\{z_{mj}x_{(m-\tau)j}^T\}, \quad \tau = 0, 1, 2, 3, \dots, \quad (2)$$

where z refers to the corresponding raster scan in the desired image.

These autocorrelation and cross-correlation functions form the basis from which a filter is derived that best, in a least-squares sense, convolves the input scene into the output scene. That is, if the best-fit filter for raster scan k (where $1 \leq k \leq n$) is defined as

$$f_k \equiv f_k(s) = \begin{bmatrix} f_{k11}(s) & f_{k12}(s) & \cdots & f_{k1p}(s) \\ \bullet & \bullet & \bullet & \bullet \\ f_{kn1}(s) & f_{kn2}(s) & \cdots & f_{knp}(s) \end{bmatrix}, \quad (3)$$

where m and n are defined as before, p is the length of the filter, and $s = 0, 1, 2, \dots, (p-1)$, then each element y_{ij} of the actual output scene y is given by

$$y_{ij} = f_{j0}x_{ik} + f_{j1}x_{(i-1)k} + f_{j2}x_{(i-2)k} + \cdots + f_{js}x_{(i-s)k}, \quad (4)$$

where $i = 1, 2, \dots, m$, $j = 1, 2, \dots, n$, $k = 1, 2, \dots, n$. The error between the desired output and the actual output is simply the difference between the desired output and the actual output. It is this error, normalized in the usual sense, that we wish to minimize in a least-squares algorithm. Each set of filter coefficients (f_{ks}) can be obtained by solving p sets of simultaneous equations given by

$$\begin{aligned} f_{k0}\Phi_{zrk}(0) + f_{k1}\Phi_{zrk}(-1) + \cdots + f_{ks}\Phi_{zrk}(-s) &= \Phi_{zrk}(0), \\ f_{k0}\Phi_{zrk}(1) + f_{k1}\Phi_{zrk}(0) + \cdots + f_{ks}\Phi_{zrk}(1-s) &= \Phi_{zrk}(1), \\ \bullet & \bullet \\ f_{k0}\Phi_{zrk}(s) + f_{k1}\Phi_{zrk}(s-1) + \cdots + f_{ks}\Phi_{zrk}(0) &= \Phi_{zrk}(s), \end{aligned} \quad (5)$$

where $1 \leq k \leq n$. These sets of normal equations form a block Toeplitz matrix and can be solved with relative ease using one of a number of efficient algorithms. Robinson (1983) provides an excellent discussion of one such method.

APPLICABILITY OF WIENER THEORY TO IMAGE DATA

Applicability of multichannel Wiener filtering to the current data set is dependent upon a series of

assumptions that must be shown to be reasonable with respect to image data. As Robinson (1983) notes, the extent to which results of the filter can be applied depends upon the extent to which these assumptions are satisfied by the input data. Four assumptions are considered here: 1) that the image data analyzed conform to statistical stationarity (that is, statistical properties of the data do not vary greatly over the scan), 2) that mean square error between the input and output sequences represents an optimal criterion to evaluate the filter, 3) that the derived filter is a linear operation and is of finite length, and 4) that adjacent pixels in the image in fact display some degree of statistical dependence. Before these assumptions are discussed, however, the nature of the noise associated with these images needs to be addressed. The two major sources of noise are the noise associated with the amplifier and the thermal noise associated with the surface signal. Both of these sources of noise are uncorrelated with signal and displays purely additive characteristics (as opposed to multiplicative). For example, examination of scans that cross low intensity and high intensity show similar variance structure when examined visually. If noise were multiplicative, the variance structure would be expected to be dissimilar over these features.

Assumption 1

The first assumption is that the statistical properties of the input sequence X_{mn} and the desired output sequence Z_{mn} (which in this case consist of rows and columns of pixels in the unfiltered and the filtered passive microwave scene) do not change with position within the portion of the scene being analyzed. This assumption, which is an adaptation of the theory of statistical stationarity applied commonly to time series, implies that the probability of encountering any specific intensity value at a pixel location is not tied to a specific origin and that the scene being analyzed is conceived to be effectively infinite in extent (adapted from Wadsworth et al., 1953). Visual examination of individual raster scans of the input test images (Figs. 2 and 5) presented in this study suggests that the range of variability is reasonably uniform both along individual rows (along image scans) and down successive image columns. Statistics that describe variation in pixel intensity

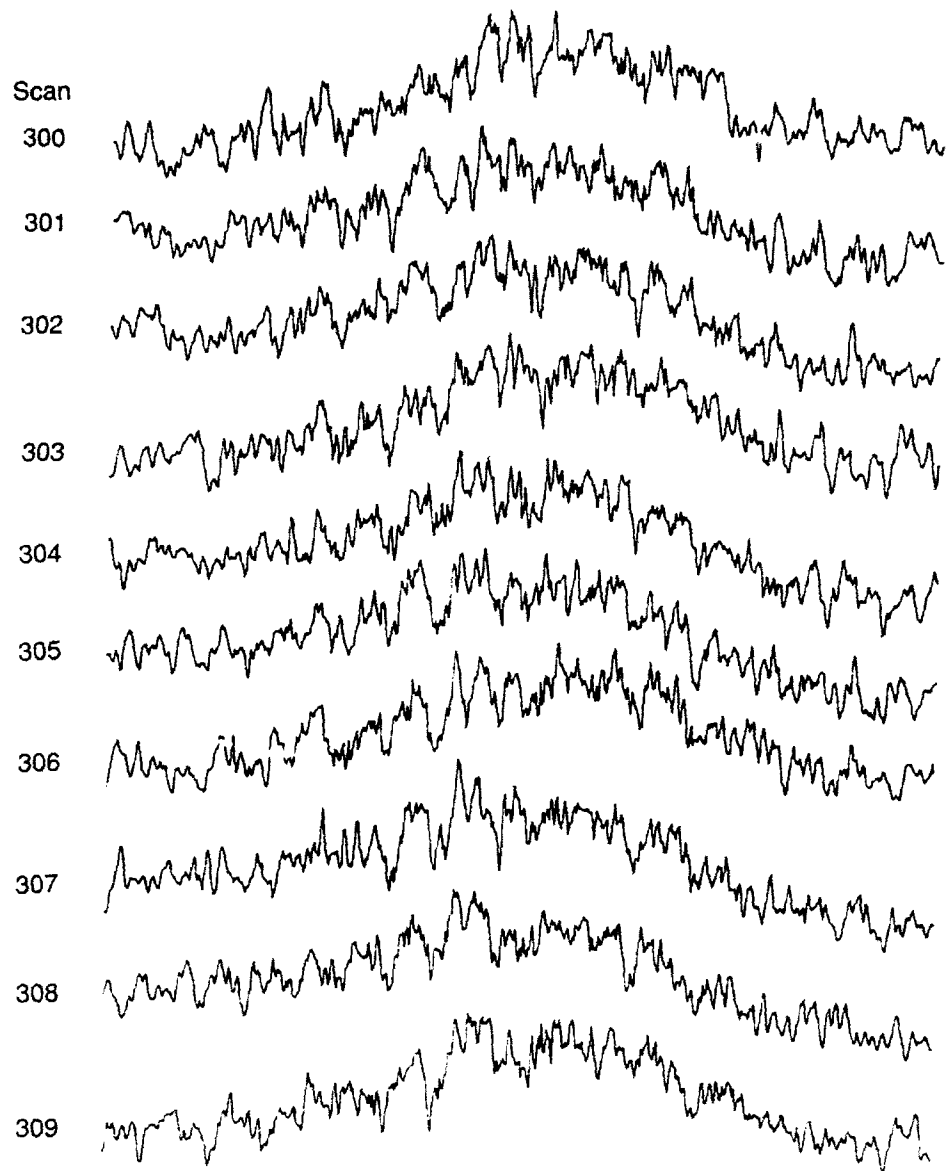


Figure 5. Plots of scans 300–309, each 512 pixels wide, from the KRMS image shown in Figure 1. Peaks and valleys that represent major features can be followed readily from scan to scan.

within and between scans support this conclusion (Tables 1 and 2).

Assumption 2

The second assumption is that the mean square error between X_{mn} and Z_{mn} is the optimal criterion to evaluate performance of the filter operators (f_0, f_1, \dots) determined in the analysis. This is similar to assumptions associated with regression analysis, principal component analysis, and least-

squares procedures in general. Conditions under which this assumption is violated occur either when the statistical variability is correlated spatially within an image, or when the autocorrelation function exhibits a paucity of correlatable events. Given the character of image data considered here, we find no compelling reason why this assumption should not hold. Tables 1 and 2 indicate that the data are not spatially correlated. Additionally, Nyquist sampling used to acquire the data produces overlap in information con-

Table 1. Statistics for Radiances in Randomly Selected Image Columns

Column	Minimum Radiance (K)	Maximum Radiance (K)	Mean Radiance (K)	Standard Deviation
9	220.0	235.0	228.1	2.6
13	221.1	233.8	228.4	2.4
39	219.3	233.5	226.5	2.5
43	221.7	233.0	226.7	2.3
60	220.1	234.1	226.0	2.4
62	221.2	233.2	226.2	2.3
68	219.5	231.1	226.7	2.5
74	216.4	232.0	226.2	2.4
81	219.2	230.6	225.9	2.1
82	216.9	230.6	225.7	2.3
89	214.5	232.3	225.5	2.5
99	215.0	230.3	225.0	2.7
101	217.4	230.9	224.8	2.6
109	216.9	231.7	224.3	2.8
120	219.1	231.1	224.5	2.6

tained in adjacent pixels (Fig. 6b) (Eppler and Heydlauff, 1990) and ensures that events recorded in adjacent scans will be highly correlated.

Assumption 3

The third assumption is that the optimal filter derived by the least-square analysis is a linear operation and is of finite length. The validity of this assumption relative to passive microwave measurements cannot be completely demonstrated. This assumption probably is valid for the relatively simple images of first-year sea ice to

Table 2. Statistics for Radiances in Randomly Selected Image Rows

Row	Minimum Radiance (K)	Maximum Radiance (K)	Mean Radiance (K)	Standard Deviation
3	219.5	233.2	226.4	2.9
13	219.3	231.4	227.5	2.5
46	222.7	235.0	229.0	2.4
49	219.6	233.7	227.1	3.3
56	220.3	231.2	226.9	2.5
70	220.7	232.2	226.1	2.5
83	221.5	230.8	226.1	2.2
91	220.6	231.7	225.8	2.1
92	221.5	230.0	226.2	2.0
100	222.5	232.3	226.5	2.4
103	220.7	229.2	225.3	2.1
107	220.2	229.7	225.1	1.7
108	220.5	230.8	225.4	2.1
115	220.5	230.5	225.5	2.2
124	215.8	232.9	225.4	3.4

which we apply the method here. Conceivably, nonlinear operators may prove to be of greater usefulness when complex scenes that include multiple surface types are analyzed, especially those scenes in which larger-scale variability over short distances is juxtaposed with (and independent of) small-scale textural patterns.

Assumption 4

The final assumption, and probably the most important one, is that adjacent pixels display some degree of statistical dependence. Dependence between successive observations is one of the fundamental characteristic of time series data (Wadsworth et al., 1953). Application of Wiener techniques to data that lack such correlation produces unpredictable results. The inherent structure and scale of image data analyzed here guarantees that a certain degree of dependence exists between adjacent pixels, both because the data are sampled robustly with respect to overlap (Eppler and Heydlauff, 1990) and because features that define the signal extend over areas of the image large enough to encompass multiple pixels.

Each observation (pixel) represents the measurement of microwave emission integrated over an elliptical area, the size and shape of which depends on viewing angle of the sensor (Fig. 6a). A significant fraction of the information carried in adjacent pixels is redundant because raw data are collected and sampled such that footprints of adjacent pixels overlap (Eppler and Heydlauff, 1990). The radiometer signal is oversampled in the along-scan direction (across image rows) such that the footprint of each pixel overlaps that of its neighbor by approximately 80% (Fig. 6b). Ground swaths of adjacent scans in test images used in this study overlap by approximately 40%, meaning that the footprint of adjacent pixels overlap by a similar amount in the across-scan direction (down image columns).

METHODOLOGY

KRMS Characteristics

Imagery used here was acquired in March 1988 in the Beaufort Sea region of coastal Alaska using the K_a-band Radiometric Mapping System (KRMS)

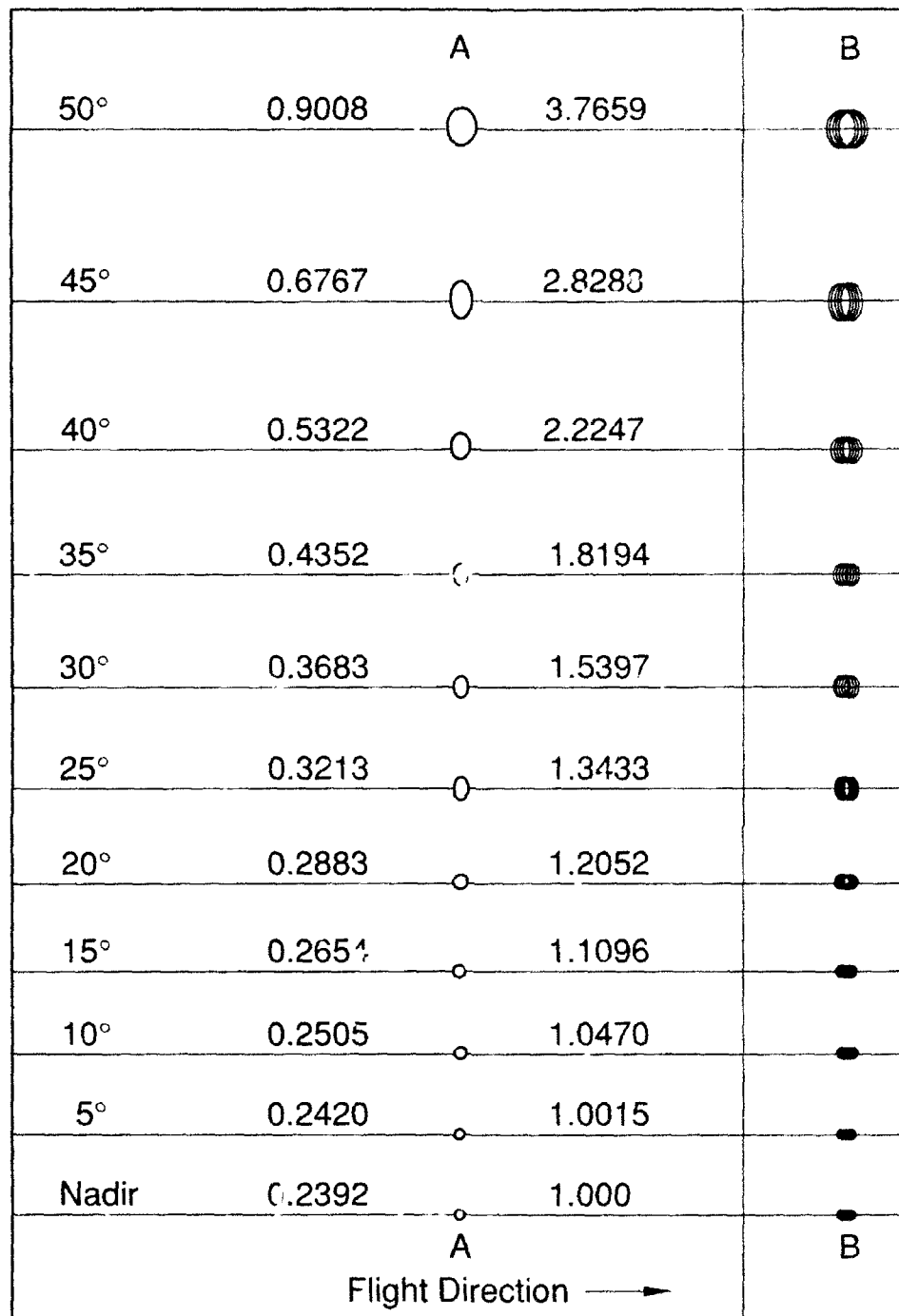


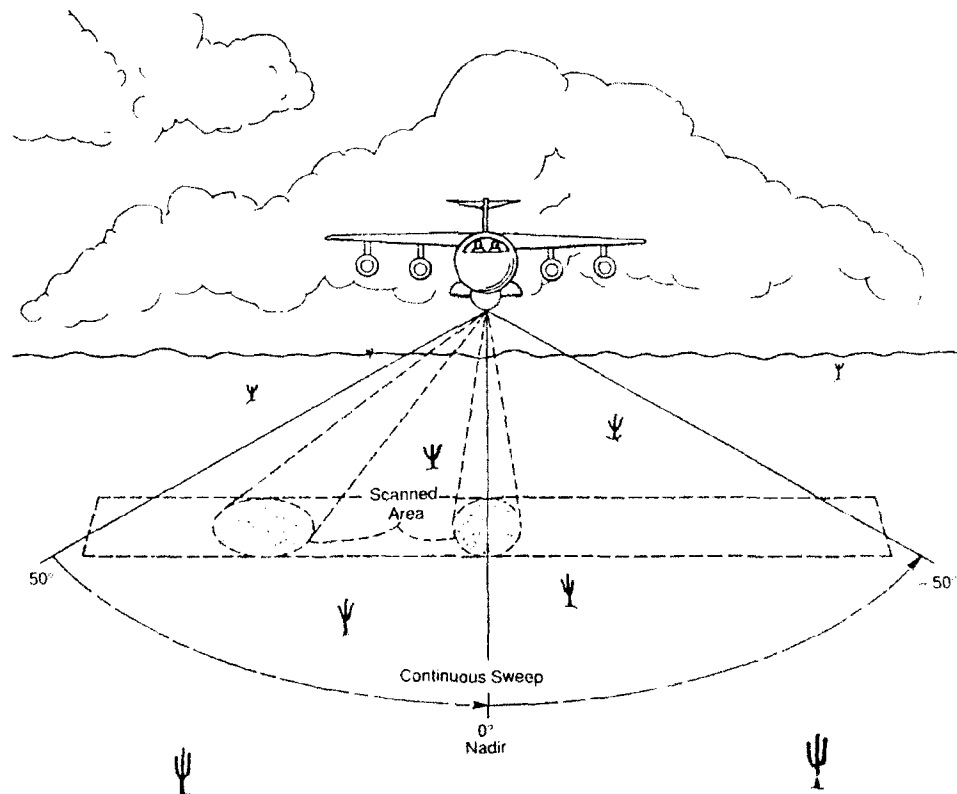
Figure 6. A) Variation in the size and shape of the KRMS 3 dB beamspot as a function of look angle. The beam, which subtends a circular spot at nadir, subtends an elliptical spot at off nadir angles. Beamspots are plotted to scale. Two conversion factors are given for each angle. The left number, when multiplied by aircraft altitude, gives the area of the beamspot in square units of altitude. The area subtended by the nadir beamspot from 10,000 ft altitude thus is 2392 sq ft. The right number represents the relative area of the beamspot with respect to the area of the nadir beamspot. The area imaged by each beam at 50° thus is 3.7659 times larger than the area imaged at nadir. B) Overlap between beamspots in adjacent KRMS scans plotted for different look angles. KRMS antenna scan rate is adjusted with respect to downtrack aircraft motion as data are collected such that the beam in each successive scan sweeps a ground swath that, at nadir, includes 80% of the area imaged in the previous scan. Overlap at off nadir angles is greater than 80% because the size of the beamspot increases with look angle.

in conjunction with the Navy-NASA SSM/I Validation Experiment (Farmer et al., 1989; Eppler and Farmer, 1991a; Cavalieri et al., 1991). KRMS is an airborne passive microwave imaging system that senses vertically polarized radiation emanating from the Earth's surface at a center frequency of 33.6 GHz. In its present configuration, the KRMS antenna assembly is enclosed in a pod that hangs either from the bomb-bay or wing of a P-3 class aircraft. Three parabolic antennas, mounted 120° apart on a single shaft within the pod, rotate about a horizontal axis that is parallel to the direction of flight. Only the signal from the downward-facing antenna is sampled and recorded at any given time. Scan is across track in a vertical plane and provides coverage of 50°, both sides of nadir (Fig. 7). The rate at which the antenna assembly rotates is controlled by the operator in the aircraft cabin and is set based on altitude and ground speed to provide 80% overlap between

successive scans. Antenna beam width is 1°, so that spatial resolution of the unprocessed signal is approximately 16 ft per 1000 ft of flight altitude at nadir. Radiometric sensitivity measured in the laboratory is 0.05 K/s; operational sensitivity is estimated to be 0.5 K or better. Additional information concerning technical characteristics of the KRMS sensor is provided by Eppler et al. (1984; 1986).

Raw data are recorded on analog tape and converted to digital form after the aircraft mission is complete (Eppler and Heydlauff, 1990). Digitized images are 512 pixels wide. Analog data are sampled to provide 80% overlap between adjacent pixels. Each row of 512 pixels corresponds to one scan by a single antenna across the full 100° field of view. Successive lines contain radiances derived from a different one of the three antennas which repeat in sequence (i.e., 0, 1, 2, 0, 1, 2, 0, 1, and so forth).

Figure 7. Scan geometry of the KRMS sensor. The downward-looking antenna assembly rotates and scans a 100°-wide swath beneath the aircraft centered on nadir. Forward motion of the aircraft moves the footprint of successive swaths farther along track. Rotation rate of the antenna is set such that one swath overlaps the next by 80% at nadir. The incidence angle from which the antenna views the surface varies with position along a scan.



Test Data

Three test images of first-year sea ice, each 128×128 pixels in size (Fig. 2), were extracted from the central portion of a full KRMS scene (512×512 pixels). These smaller 128×128 -pixel images were used instead of the full 512×512 -pixel images, both to reduce computation time and to minimize cross-track variance in microwave radiance. Microwave emissivity varies as a function of the incidence angle from which a surface is viewed. Part of the variance observed in KRMS data results from changes in look angle from pixel to pixel across the 100° field of view. Cooler brightness temperatures (lighter tones) observed down the central section of Figure 1 as compared with warmer temperatures (darker tones) at image limbs result from differences in the angle at which KRMS antennas view the ice surface (Fig. 7). Theory predicts and field experiments show that, for vertically polarized radiation, the scale of this variation is smallest at near-nadir angles where look angle is almost perpendicular to the surface (Fig. 8) (Kong et al., 1979; Fung and Chen, 1981; Stogryn, 1981; Eppler et al., 1984).

KRMS scans (image rows) were sampled to extract the middle 128 pixels (pixels 192–320) so that scene nadir falls between the middle two columns of each test image (columns 64 and 65). Look angle at the extremes of these test images is approximately 13° . KRMS data analyzed previously suggest that the radiometric effect of changes in look angle across these central pixels is less than 2 K for first-year sea ice (Fig. 8b). Statistics that summarize minimum, maximum, and mean radiance for pixels across the test images (Table 1) corroborate these previous data and suggest that bias across the test images is not significant. If data from larger angles were included, the variance structure displayed at the ends of each row could be significantly different from that in the central portion of the scan line. This would violate Assumption 1 above, which requires that the data be stationary in a statistical sense.

Scan-to-scan changes in radiance that arise from differences between response characteristics of the three antennas were eliminated by using data derived from one of the three KRMS antennas. In effect, every third line of the full scene was sampled. This results in foreshortening of

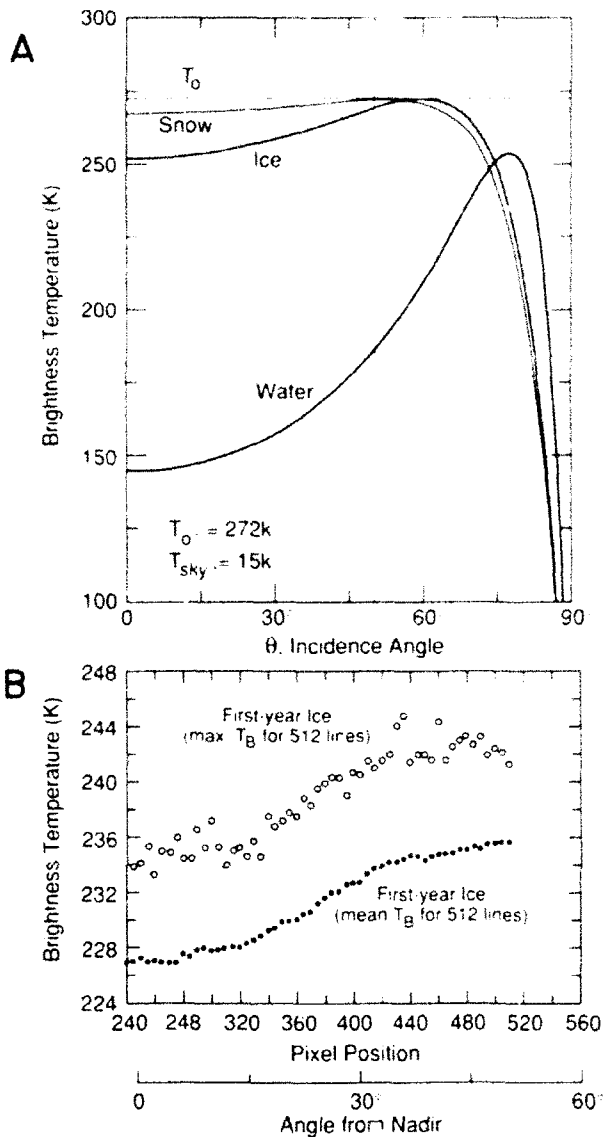


Figure 5. Vertically polarized brightness temperature as a function of incidence angle A) as predicted for sea water, fresh water ice, and dry snow by a radiometric model (from Stogryn, 1981) and B) as measured from KRMS images of first-year sea ice (from Eppler et al., 1984). The vertical dotted line in A) marks the imaging limit for full-width KRMS scenes. The image limit of test scenes used here is approximately 13° . T_0 is ambient air temperature and T_{sky} is sky temperature used in the model calculation.

image geometry by a factor of 0.33, and reduction of overlap between adjacent pixels in the down-column direction from 80% to 40%. Overlap, although reduced, remains sufficient to ensure statistical dependence between adjacent pixels (Assumption 4 above). Scene geometry and overlap in the across-row direction remains unaffected.

APPLICATION OF THE WIENER FILTER

In applying the Wiener technique to the three test images in Figure 2, we evaluated the effect of altering values assigned to four key variables used to design any given Wiener filter: 1) lag [τ in Eqs. (1) and (2)] or the number of pixels the original scene is offset to define the desired signal; 2) length of the final filter [ρ in Eq. (3)]; 3) number of lines (channels) to include in the filter (n , an arbitrary choice); and 4) degree of weighing applied to the empirical correlation functions (both autocorrelation and cross correlation) in the estimate of the true correlation (Robinson, 1983). In the present situation, another option is to define filters that are applied either parallel to the scanning direction (across the image), or perpendicular to the scan direction (down the image).

The evaluation scheme we will apply involves mainly visual appraisal of the processed image. That is, does one combination of variables "look" any better in terms of presenting desired information than another combination? Statistics such as root mean square are calculated that are useful for relative comparisons (Robinson, 1983), but it is ultimately the visual clarification of the textural components in each scene which drives this analysis. The results presented below were selected from many combinations of lag, length, weight, and number of included lines that were tried.

Lag

Figure 9 presents the original three scenes and the results of applying a filters with lags of 1, 2, 3, and 5 pixels. The filter length was held at a constant length of 25 pixels for all scenes. Additionally, three channels were incorporated in the filter design, no weighing was used, and the images were processed parallel to the scan lines. These images, and all subsequent images, are presented in histogram equalized format and intensity stretched to cover the possible range of intensities. This processing enhances subtle features. Figure 10 presents the original images minus the processed image, also equalized and stretched as previously described. Such presentation (Fig. 10) is useful for determining what effect, if any, a particular filter had on the original image.

Figures 9 and 10 show that increasing the lag

between the original and desired scene removes apparent noise of increasing spatial scale. That is, the greater the lag, the greater the scale of noise that is minimized. Additionally, at low values of lag energy associated with sharp intensity changes is smeared over a larger region than for large lags as is evident in the first column of images that show a bright feature near the image center. Figure 10 more clearly shows the enhancement of progressively longer events at the expense of the higher frequency information.

Length

Figure 11 presents the results of applying filters with lengths of 3, 5, 7, and 10 pixels. The lag was held to 1, the number of lines (channels) was 3, and no weights were applied. Figure 12 displays the original minus filtered images for comparison. Visually, the advantage of using longer than 3-pixel-length filters is difficult to ascertain in this case as it appears that the majority of the noise reduction was accomplished with shorter filters. It is interesting to note that filters in the range of 3-5 pixels correspond roughly to the amount of average signal overlap contained in each scan, which is in alignment with the assumptions associated with the application of Wiener theory. Very little improvement is realized with increased filter length, suggesting that, at least on the scale of variability shown in these images, significant enhancement can be obtained using relatively short filters. However, examination of the normalized root mean square error associated with a given filter length (Table 3) suggests that, at least relative to the case described above, the majority of the decrease in this error is accomplished with a filter length of 12 pixels and under. This is more clearly demonstrated in Table 4, which depicts the amount of change in the normalized root-mean-square error as filter length is increased. Further examination of Tables 3 and 4 indicate that the same is generally true for lags of 2 and 3 pixels whereas filters defined for longer lags would benefit by an increased filter length.

Lines (Channels)

Changing the number of lines (channels) used to define the Wiener filter produced results displayed in Figures 13 and 14. The number of lines

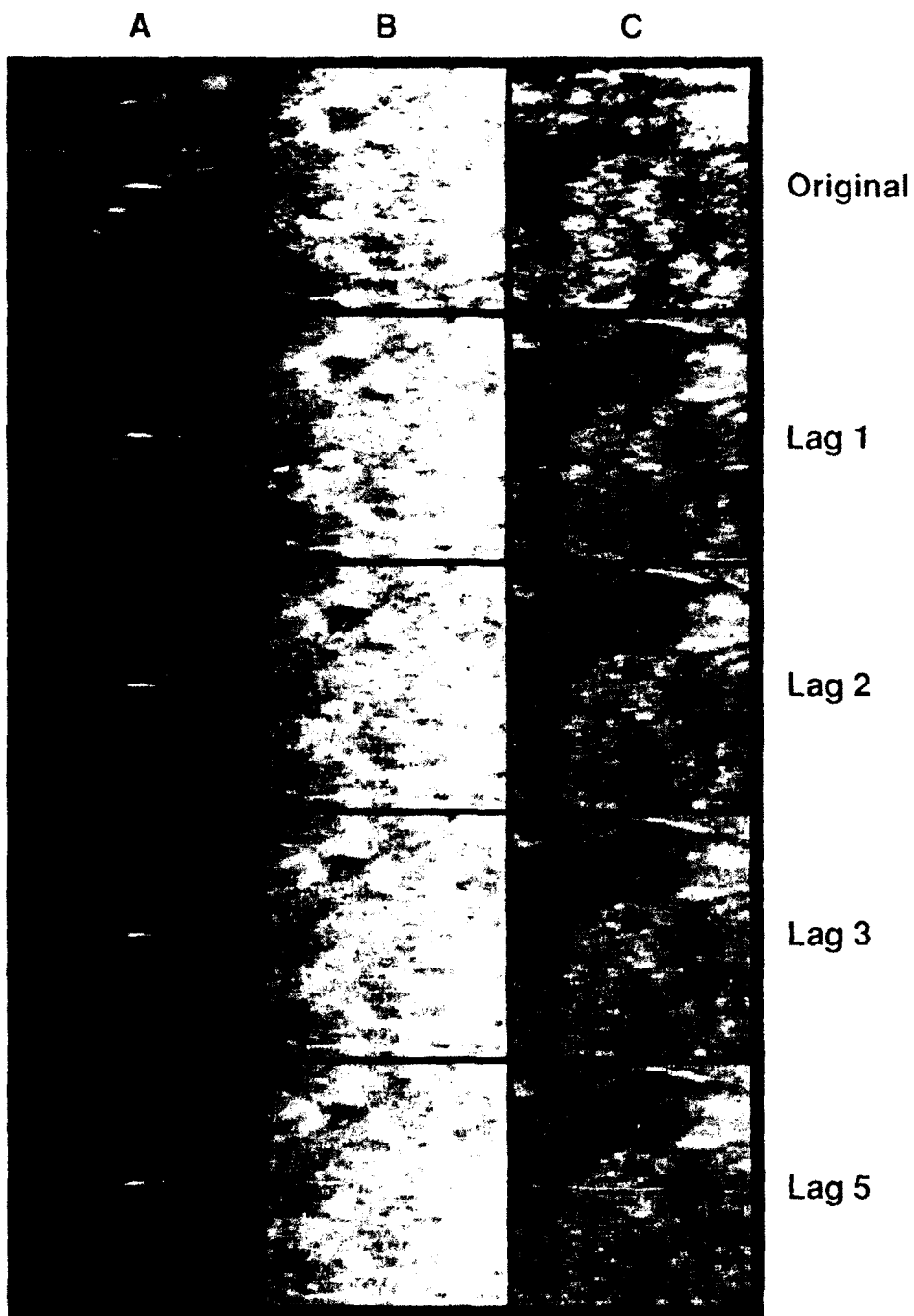


Figure 9. Effects of using lags of different magnitude in Wiener-filtered images. Unfiltered images are shown in the first row (original). Images filtered with shifts of 1, 2, 3, and 5 pixels in the horizontal direction (lag = 1,2,3,5) are shown in successive rows. Filter length was held constant at 25 pixels, three adjacent lines were used to define a filter operator, no weighing applied, and processing was parallel to the scan direction (horizontal in these images). Note that as lag increases, longer wavelength features are enhanced while shorter wavelength features are minimized.

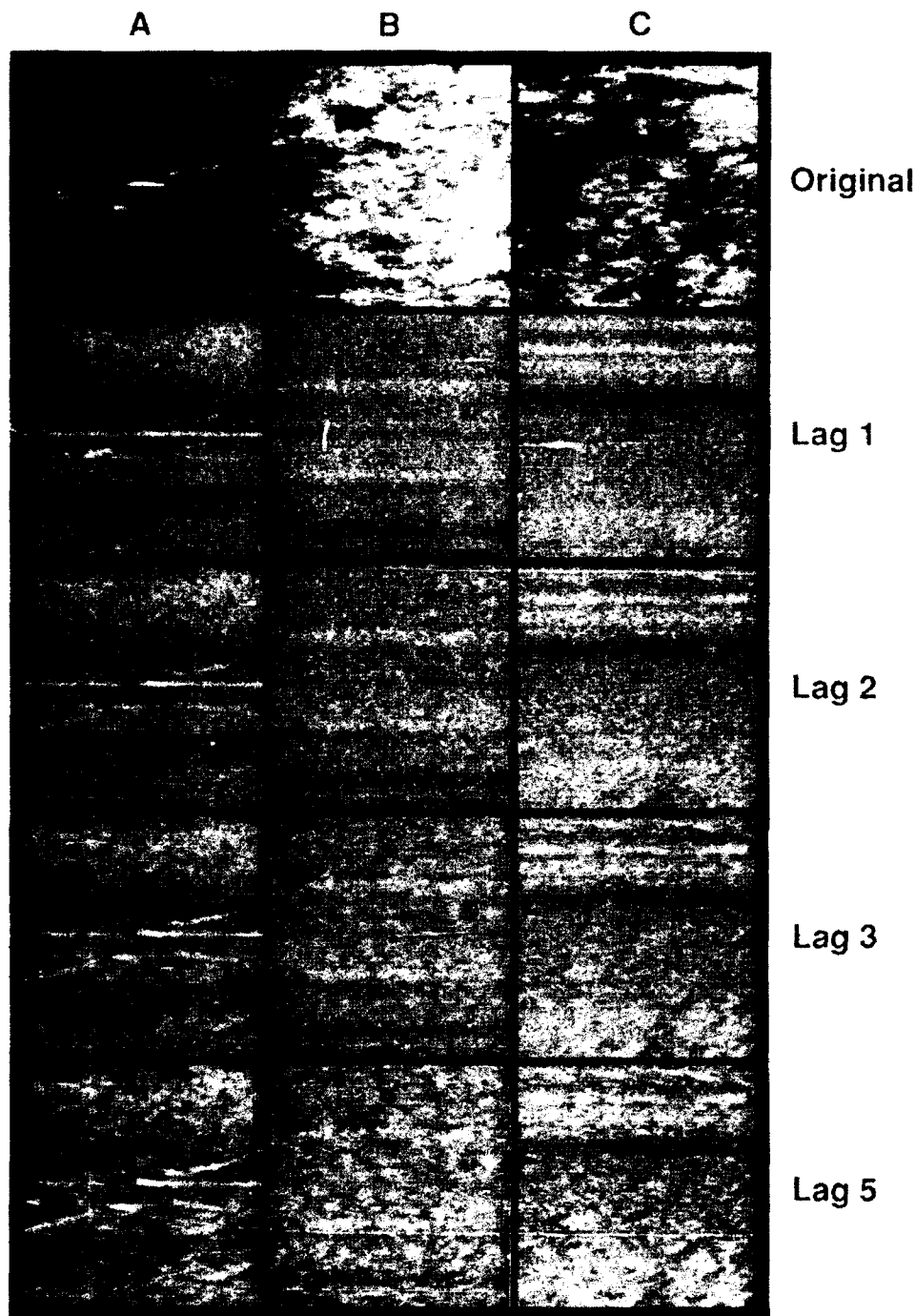


Figure 10. Difference images derived by subtracting the filtered images in Figure 9 from the unfiltered images (first row). Features that appear in these different images represent information removed from the unfiltered scenes.

used in each row of images varied from 1 to 10. The lag was 1 for all images, the length of the filter was 25, and no weights were applied. Since Wiener theory relies on the autocorrelation and cross-correlation functions, highly correlatable events will tend to dominate design of the opti-

mum filter. Such cases arise in our data along the edge of clearly defined features, in the vicinity of a textural change, or at abrupt changes in intensity. The net result is that the greater the number of lines used in the analysis, the blockier the filtered image appears to be in Figure 14. Also

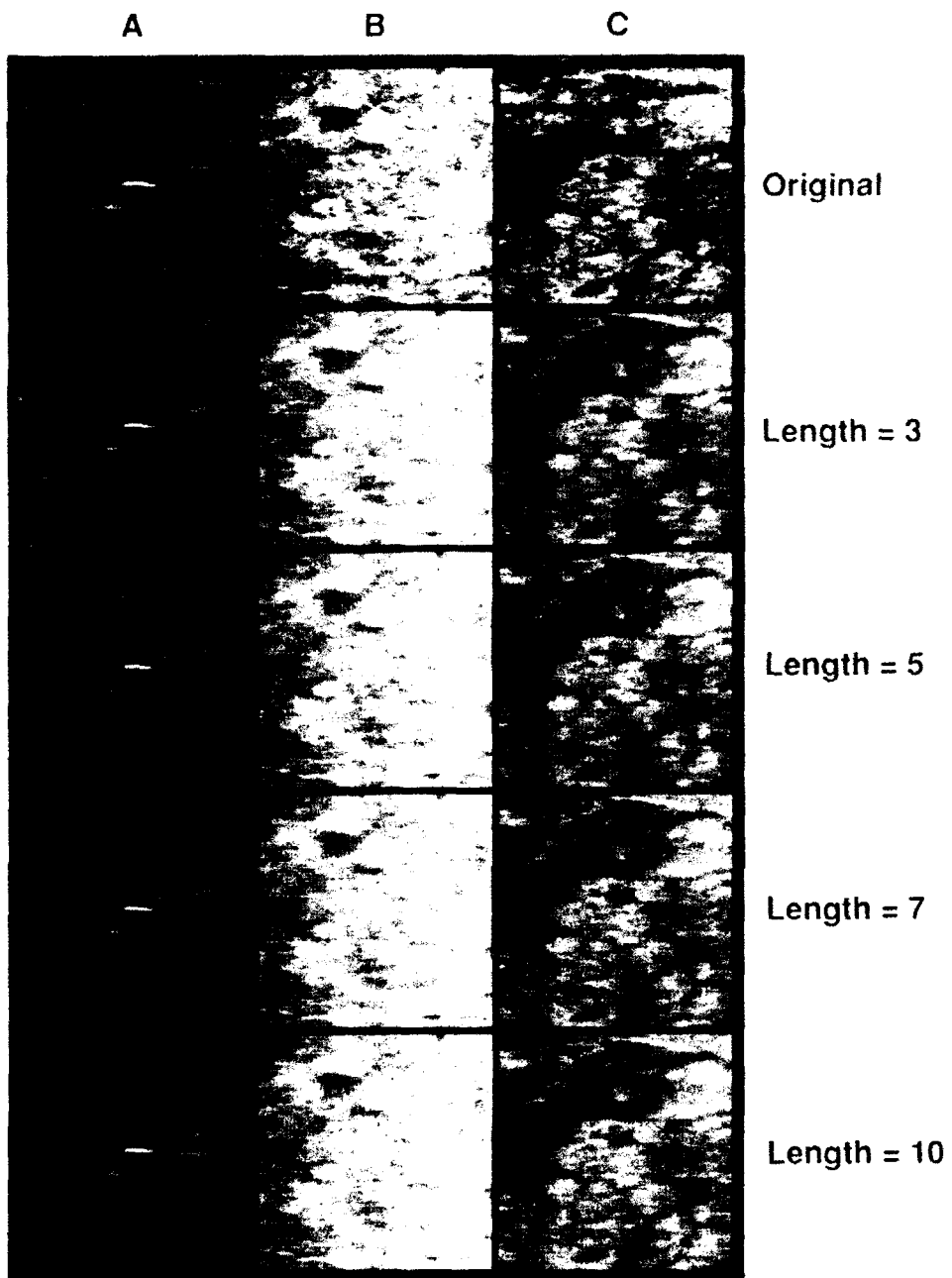


Figure 11. Effect of using Wiener filters of different length (3, 5, 7, and 10 pixels). Lag was one pixel, three lines were used, and no weighing function was incorporated. Note the lack of visually significant changes as increasingly longer filter operators are applied.

noted in these images is the tendency of filters composed of larger numbers of lines to enhance the more dominant, correlatable events in a scene, which are defined by a larger number of lines. This results in less enhancement of smaller-scale features which are defined by relatively few lines. Using two or three channels in the filter design would roughly correspond to the average amount

of overlap among adjacent scans, which, as noted before, corresponds to the assumptions which underlay this analysis.

Weight

Changing the weighing function (Figs. 15 and 16) produced no visually significant differences. The

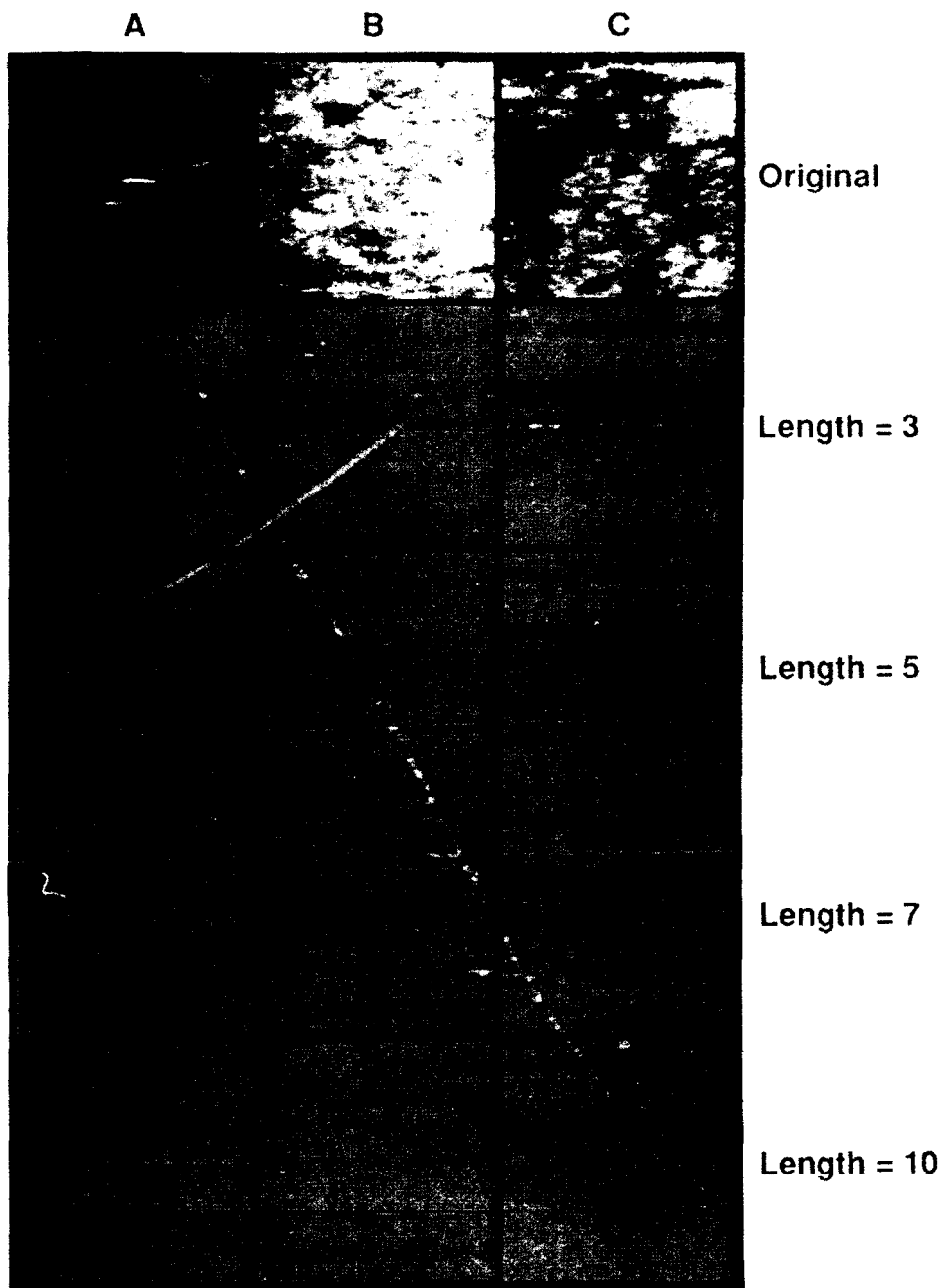


Figure 12. Difference images derived from subtracting the filtered images in Figure 11 from the unfiltered images (first row). Only subtle changes are observed as filter length increases.

lag was 1, the length was 25, and three lines were included in the filter. The weighing function values displayed in these images include 0 (no weights), 10 (maximum weighing), and 30 and 50 (intermediate weights) [weighing scale defined in Robinson (1983)]. The conclusion we draw from these images is that weighing for the correlation function is not a visually significant variable to

consider for this type of image data. Further analysis may be warranted when the image displays different variance-covariance structures.

Scan Direction

Finally, scenes were processed both parallel to the scan direction and perpendicular to the scan

Table 3. Filter Length and Normalized Root-Mean-Square Error Values for Systems of 1, 2, 3, 4, and 5 Lag Pixels Presented for Filter Lengths up to 25 Pixels^a

Filter Length	Normalized Root Mean Square				
	Lag = 1	Lag = 2	Lag = 3	Lag = 4	Lag = 5
1	0.339	0.372	0.425	0.492	0.579
2	0.304	0.343	0.408	0.476	0.568
3	0.293	0.337	0.393	0.470	0.559
4	0.288	0.319	0.386	0.455	0.539
5	0.269	0.311	0.377	0.436	0.504
6	0.266	0.305	0.362	0.419	0.474
7	0.260	0.295	0.345	0.388	0.458
8	0.253	0.283	0.321	0.374	0.443
9	0.241	0.261	0.303	0.357	0.422
10	0.230	0.249	0.298	0.349	0.404
11	0.218	0.244	0.290	0.336	0.394
12	0.210	0.240	0.280	0.332	0.389
13	0.208	0.233	0.273	0.325	0.383
14	0.202	0.227	0.268	0.320	0.375
15	0.197	0.224	0.262	0.313	0.363
16	0.193	0.219	0.256	0.300	0.350
17	0.188	0.215	0.250	0.294	0.342
18	0.184	0.210	0.244	0.282	0.330
19	0.178	0.205	0.237	0.273	0.316
20	0.176	0.199	0.227	0.262	0.297
21	0.171	0.192	0.218	0.244	0.291
22	0.167	0.185	0.207	0.234	0.270
23	0.161	0.178	0.198	0.226	0.260
24	0.153	0.171	0.191	0.214	0.238
25	0.148	0.167	0.186	0.201	0.226

^a These values are recorded for the first set of scan lines in the first image and are typical for the majority of the scans in each image. There were three scan lines used to define each filter.

direction. No visually significant differences between images were observed except that the scenes processed parallel to the scan lines seemed a little sharper than those processed perpendicular to the scan lines. This may be due to the fact that there is a larger correlation between adjacent pixels along a scan than there is between adjacent pixels in two scans simply based on amount of oversampling by the instrument.

DISCUSSION

The application of multichannel Wiener theory to passive microwave images of first-year sea ice has produced visually sharper images. That is, the filtered images appear to be more focused than the original images. The advantages of the Wiener-processed images are that textural features are enhanced, and high frequency noise is reduced. The disadvantages are that this filter in-

Table 4. Change in Normalized Root-Mean-Square Error Values for Filters of Increasing Length in Systems of 1, 2, 3, 4, and 5 Lag Pixels^a

Step	Change in Normalized Root Mean Square				
	Lag = 1	Lag = 2	Lag = 3	Lag = 4	Lag = 5
1-2	0.035	0.029	0.017	0.016	0.011
2-3	0.011	0.006	0.015	0.006	0.009
3-4	0.005	0.018	0.007	0.015	0.020
4-5	0.019	0.008	0.013	0.019	0.035
5-6	0.003	0.006	0.011	0.017	0.030
6-7	0.006	0.010	0.017	0.031	0.016
7-8	0.007	0.012	0.024	0.014	0.015
8-9	0.012	0.022	0.018	0.017	0.021
9-10	0.011	0.012	0.005	0.008	0.018
10-11	0.012	0.005	0.006	0.013	0.010
11-12	0.008	0.004	0.010	0.004	0.005
12-13	0.002	0.007	0.007	0.007	0.006
13-14	0.006	0.006	0.005	0.005	0.008
14-15	0.005	0.003	0.008	0.007	0.012
15-16	0.004	0.005	0.006	0.013	0.013
16-17	0.005	0.004	0.006	0.006	0.008
17-18	0.004	0.005	0.006	0.012	0.012
18-19	0.006	0.005	0.007	0.009	0.014
19-20	0.002	0.006	0.010	0.011	0.019
20-21	0.005	0.007	0.009	0.018	0.006
21-22	0.004	0.007	0.011	0.010	0.021
22-23	0.006	0.007	0.009	0.008	0.010
23-24	0.008	0.007	0.007	0.012	0.022
24-25	0.005	0.004	0.005	0.013	0.012

^a These values were calculated from Table 3. The step values refer to the fact that one row of Table 3 representing a given filter length is subtracted from the previous row, which reflects a filter length 1 pixel shorter. Larger values in the change columns indicate relatively larger changes in root-mean-square values with increasing filter length.

duces a slight blocky grain to the image and can produce a type of ringing along scan lines which traverse sharp intensity contrasts (discontinuous variability in the scans). The usual practice of applying tapered filter weights (Rush, 1990) to remove this ringing is not normally performed with the Wiener filter. Rather, the existence of such ringing is probably indicative of a local pixel region whose statistical structure differs markedly from the regional structure. Defining regions with similar statistical structure before the application of Wiener theory might allow the definition of a single filter that can be used for this region. This filter might be defined from previous experience or simply be the product of the first set of scan lines encountered in the defined region. In our case, the advantages outweigh the disadvantages because ice textural features that occur on intermediate scales are enhanced which is the primary objective of this study. A reasonable filter to apply in our case would consist of two or three channels,

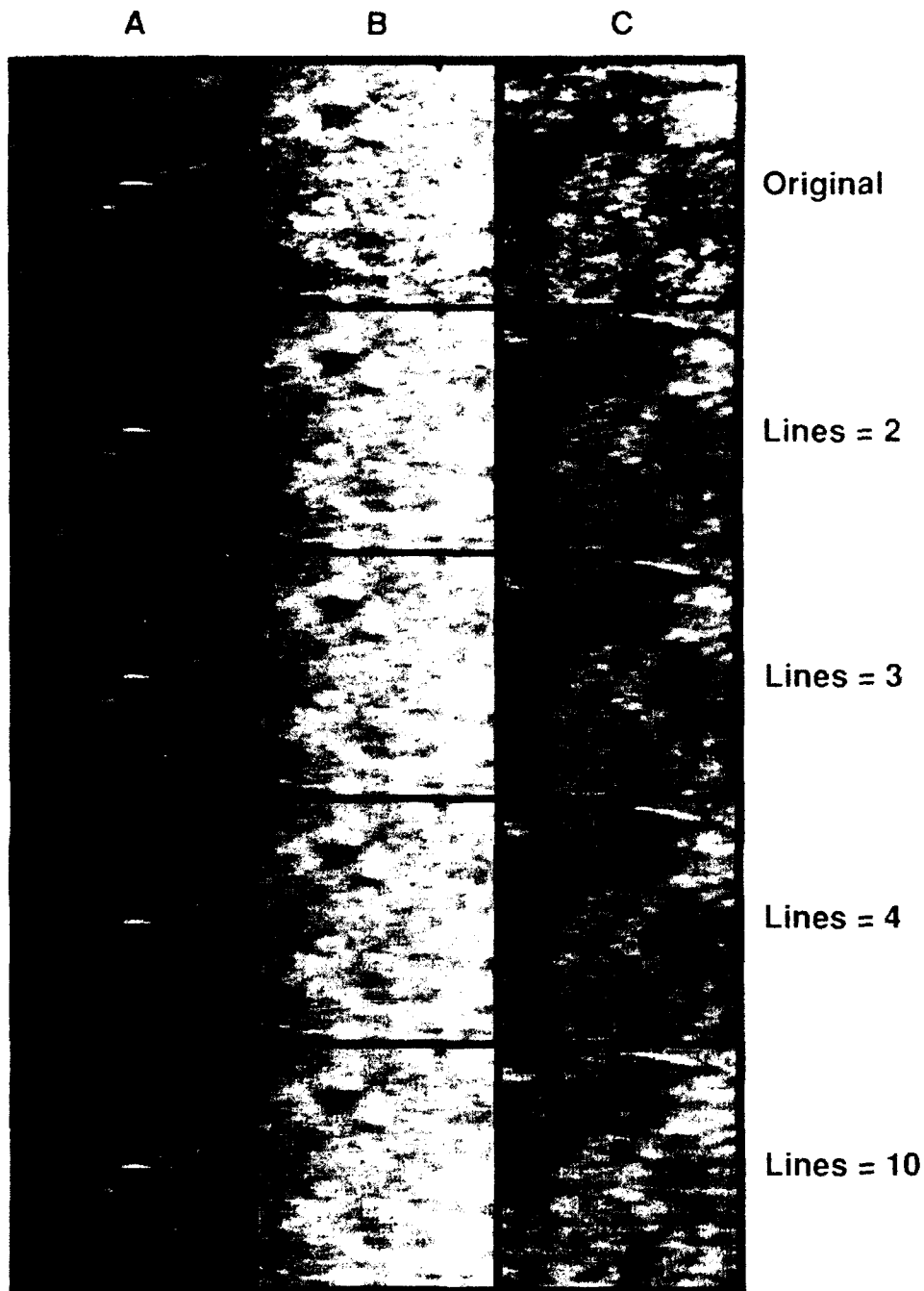


Figure 13. Effect of using Wiener filters that are composed of different numbers of scan lines (2, 3, 4, and 10). In each case, lag was one, filter length was 25, and no weighing function was used. Image texture becomes increasingly blocky as the number of lines increases.

have a lag of 1 pixel, a length of approximately 12–14 pixels, and no correlation weighing. This image would be filtered parallel to the scan direction. This combination is based on the minimum filter needed to show significant visual improvement. More complex filters have not been shown to increase visual enhancement significantly.

In terms of practical application, however, Wiener theory does have some drawbacks. For example, the Wiener algorithm, as implemented by us in this study, defines a new set of filters for each collection of scan lines. In a 128×128 scene, a three-channel filter would involve 129 separate applications of the algorithm. This approach, while

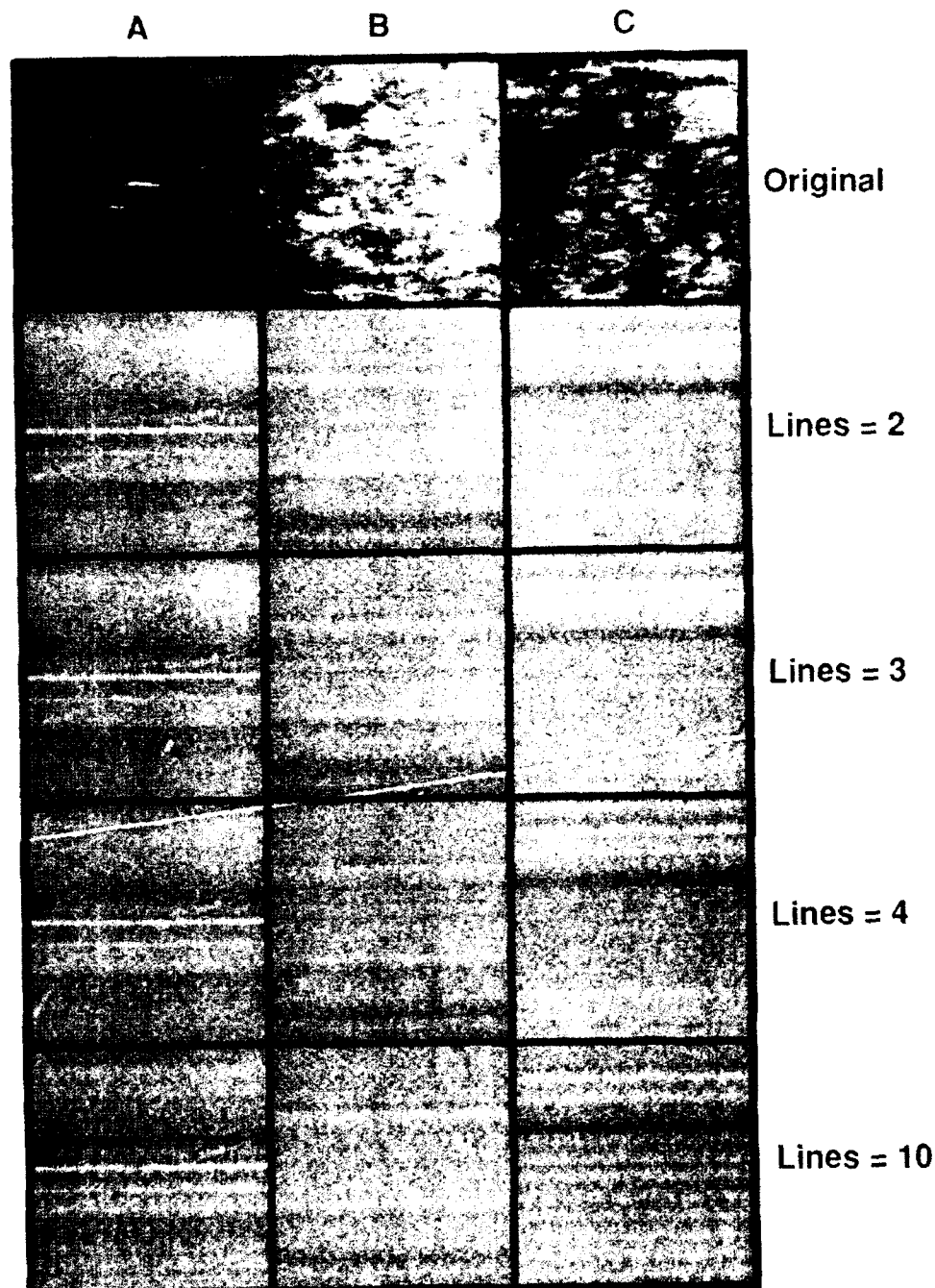


Figure 14. Difference images derived by subtracting the filtered images in Figure 13 from the unfiltered images (first row).

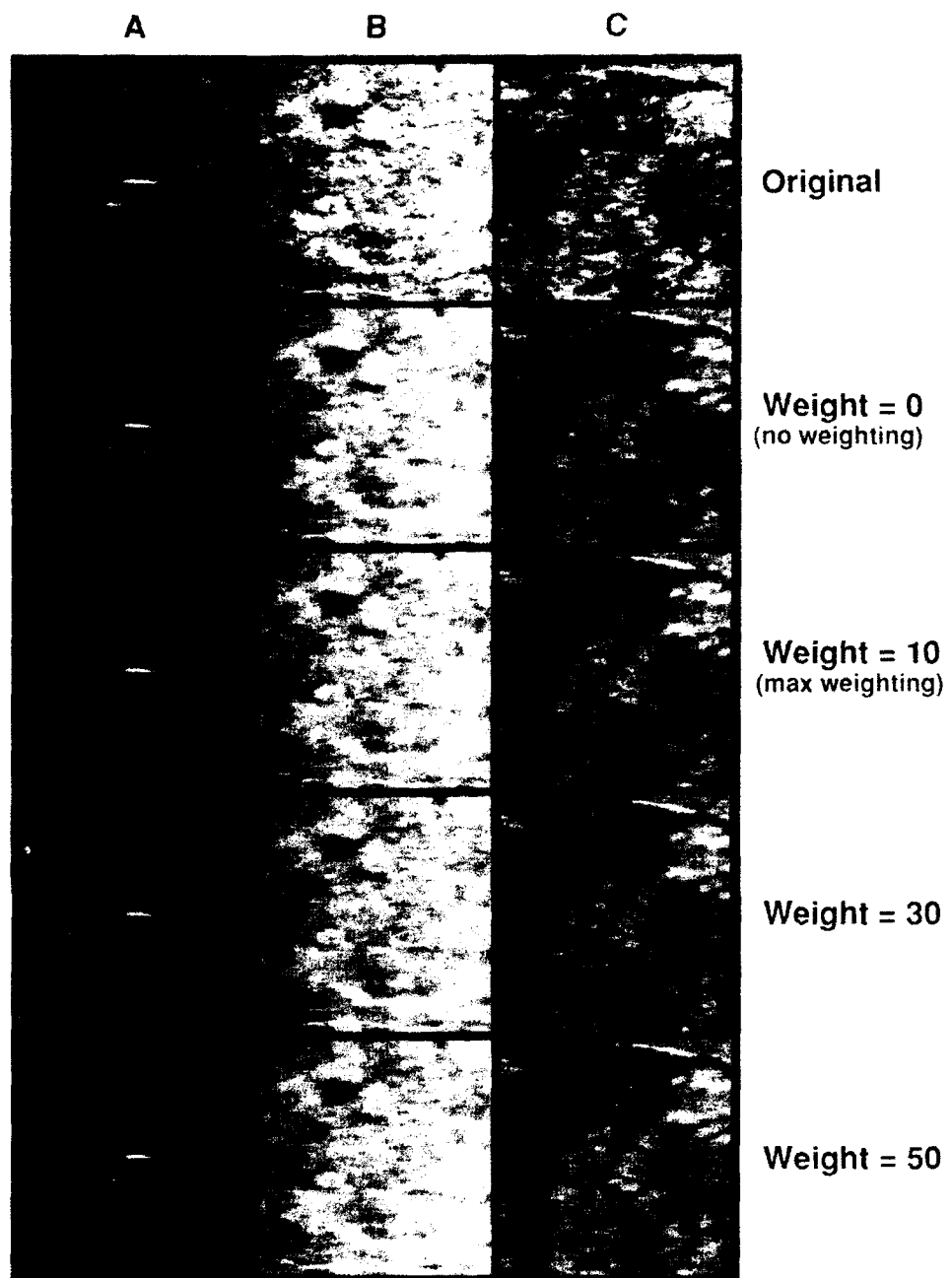


Figure 15. Effect of weighing on Wiener-filtered images: no weighing (0), maximum weighing (10), and intermediate weights (30 and 50). Lag was one pixel, three lines used for filter definition, and filter length was 25 pixels in all cases. Visually significant changes are not observed as the weighing function varies.

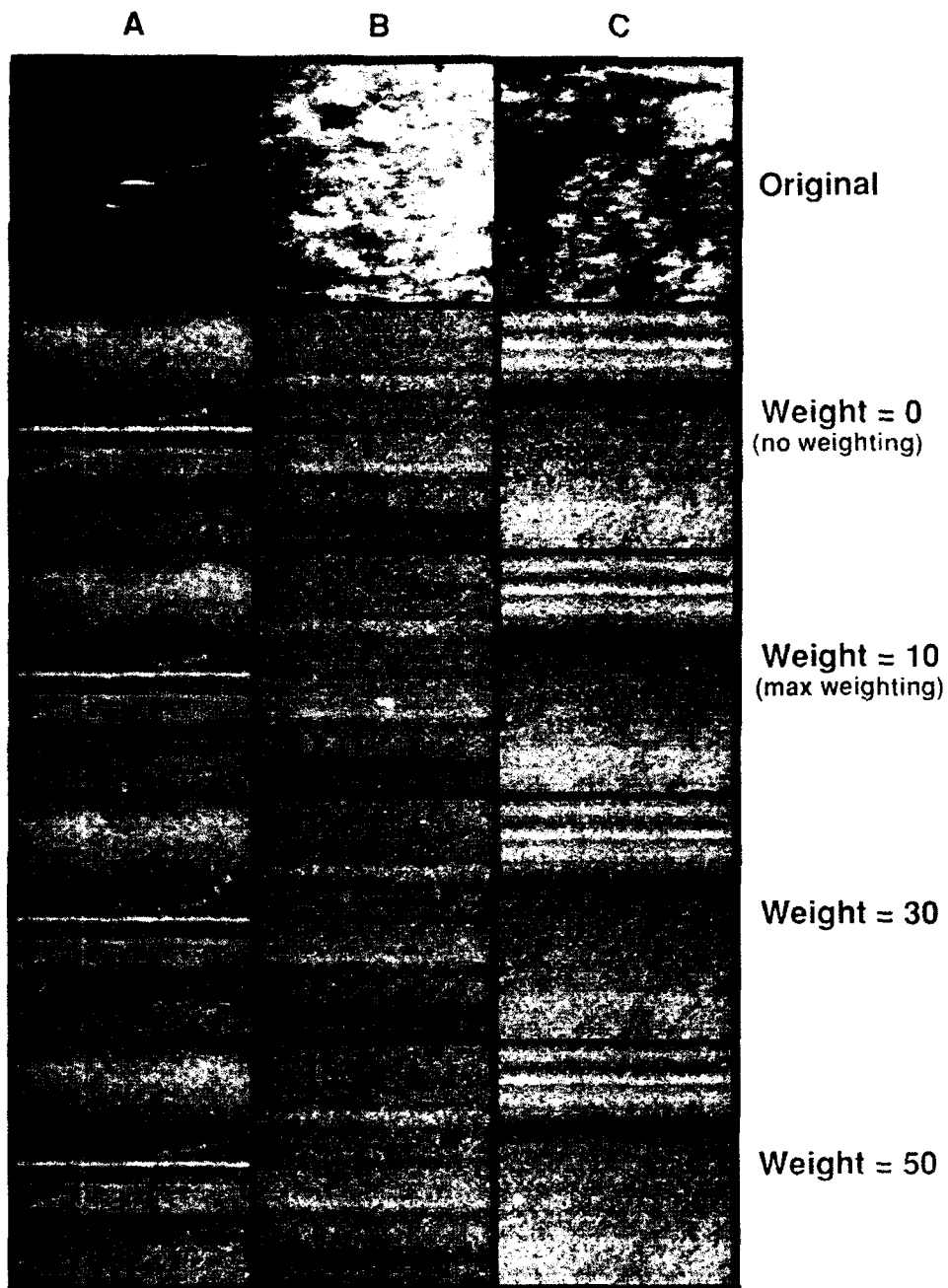


Figure 16. Difference images derived by subtracting the filtered images in Figure 15 from the unfiltered images (first row). These difference images generally support the conclusion that no visually significant differences appear when various weights are applied in the filter design.

computationally cumbersome, was chosen in order to allow the filtering scheme to be more sensitive to changes in altitude, plane position, and changes in ice type. In such an approach a single filter appropriate for a specific ice-type or ice texture would be defined. This would result in significant computational advantages. Such filters could not, however, be applied across abrupt

changes in intensity such as those associated with different ice types. The result of such an application would be the introduction of a ringing in the region of the abrupt change. If such areas were included in images used to design the filter, the resultant filter would enhance the largest and most correlatable events at the expense of smaller features, such as the more subtle texture observed

in first-year ice. This is a common problem associated with most variance algorithms and has received extensive discussion in other fields such as seismic analysis (Wadsworth et al., 1953).

Passive microwave imagery used in this study was acquired in conjunction with the joint Navy-NASA SSM/I Sea Ice Validation Experiment using funds provided both by the Oceanographer of the Navy (OP-096, project element 63704N) through the Satellite Applications Technology (SAT) Program, A.E. Pressman program manager, and by NASA through the Snow and Ice Processes Program, R. Thomas program manager. Data analysis was funded under Department of Defense program element 0601153N through the Sea Ice Classification Project and through a grant from these funds to W. E. F. W. E. F. also received support under a Summer Faculty Research Fellowship awarded by the U.S. Navy-American Society for Engineering Education Fellowship Program through NOARL's Basic Research Management Office (Code 114), H. E. Morris head. This work represents NOARL Contribution No. JA-332:019:92.

REFERENCES

Campbell, W. J., Weeks, W. F., Ramseier, R. O., and Gloersen, P. (1975), Geophysical studies of floating ice by remote sensing, *J. Glaciol.* 15(73):305-328.

Campbell, W. J., Gloersen, P., Webster, W. J., and Wilheit, T. T. (1976), Beaufort sea ice zones delineated by microwave imagery, *J. Geophys. Res.* 81(6):1103-1110.

Campbell, W. J., Wayenberg, J., Ramseyer, J. B., et al. (1978), Microwave remote sensing of sea ice in the AIDJEX main experiment, *Boundary Layer Meteorol.* 13:309-337.

Cavalieri, D. J., Gloersen, P., and Wilheit, T. T. (1986), Aircraft and satellite passive microwave observations of the Bering Sea ice cover during MIZEX West, *IEEE Trans. Geosci. Remote Sens.* GE-24(3):368-377.

Cavalieri, D. J., Crawford, J. P., Drinkwater, M. R., et al. (1991), Aircraft active and passive microwave validation of sea ice concentration from the DMSP SSM/I, *J. Geophys. Res.* 96(C12):21,989-22,008.

Eppler, D. T., and Farmer, L. D. (1991a), Navy-NASA SSM/I validation experiment KRMS data products, NOARL Technical Note 48, Naval Oceanographic and Atmospheric Research Laboratory, Stennis Space Center, MS, 49 pp.

Eppler, D. T., and Farmer, L. D. (1991b), Texture analysis of radiometric signatures of new sea ice forming in Arctic leads, *IEEE Trans. Geosci. Remote Sens.* 29(2):233-241.

Eppler, D. T., and Heydlauff, B. M. (1990), Digitizing KRMS analog data on a personal computer, NORDA Report 219, Naval Ocean Research and Development Activity, Stennis Space Center, MS.

Eppler, D. T., Farmer, L. D., Lohanick, A. W., and Hoover, M. (1984), Digital processing of passive K_a-band microwave images of sea ice, NORDA Report 51, Naval Ocean Research and Development Activity, NSTL, Mississippi, 54 pp.

Eppler, D. T., Farmer, L. D., Lohanick, A. W., and Hoover, M. (1986), Classification of sea ice types with single-band (33.6 GHz) airborne passive microwave imagery, *J. Geophys. Res.* 91(C9):10,661-10,695.

Farmer, L. D., Eppler, D. T., Heydlauff, B. M., and Olsen, D. (1989), KRMS SSM/I validation March 1988 quick look report, NORDA Technical Note 385, Naval Ocean Research and Development Activity, Stennis Space Center, MS, 43 pp.

Fung, A. K., and Chen, M. F. (1981), Emission from an inhomogeneous layer with irregular interfaces, *Radio Sci.* 16(3):289-298.

Gonzalez, R. C., and Wintz, P. (1977), *Digital Image Processing*, Addison-Wesley, Reading, MA, 431 pp.

Hollinger, J. P., Kenney, J. E., and Troy, B. E. (1976), A versatile millimeter-wave imaging system, *IEEE Trans. Microwave Theory Techniques* MTT-24:786-793.

Hollinger, J. P., Troy, B. E., Raimseier, R. O., Asmus, K. W., Hartman, M. F., and Luther, C. A. (1984), Microwave emission from high Arctic sea ice during freeze-up, *J. Geophys. Res.* 89(C5):8104-8122.

Hoyer, R. (1990), A global approach to image texture analysis, NOARL Report 238, Naval Oceanographic and Atmospheric Research Laboratory, Stennis Space Center, MS, 286 pp.

Kong, J. A., Shin, R., Shive, J. C., and Tsang, L. (1979), Theory and experiment for passive microwave sensing of snowpacks, *J. Geophys. Res.* 84(B10):5669-5673.

Robinson, E. (1983), *Multichannel Time Series Analysis with Digital Computer Programs*, 2nd ed., Goose Pond Press, Houston, TX, 454 pp.

Robinson, E. A., and Durrani, P. S. (1986), *Geophysical Signal Processing*, Prentice Hall, Englewood Cliffs, NJ, 481 pp.

Robinson, E. A., and Treitel, S. (1980), *Geophysical Signal Analysis*, Prentice Hall, Englewood Cliffs, NJ, 466 pp.

Rosenfeld, A., and Kak, A. C. (1982), *Digital Picture Processing*, Academic, New York, Vol. 1, 435 pp.

Rush, J. C. (1990), *Computer-Assisted Microscopy: The Measurement and Analysis of Images*, Plenum, New York, 453 pp.

Stogryn, A. (1981), Electromagnetic properties of random media, Technical Report TR-1, Report Number 6140, Aerojet Electric Systems Co., Asuza, CA, 115 pp.

Wadsworth, G. P., Robinson, E. A., Bryan, J. G., and Hurley, P. M. (1953), Detection of reflections on seismic record by linear operators, *Geophysics* 18:539-586.

Wiener, N. (1942), *The Extrapolation, Interpolation and Smoothing of Stationary Time Series with Engineering Applications*, MIT Press, Cambridge, MA, 163 pp.

Williams, D. F., Lerche, I., and Full, W. E. (1988), *Isotope Chronostratigraphy: Theory and Methods*, Academic, New York, 345 pp.